Journal of Zhejiang University-SCIENCE A (Applied Physics & Engineering)
ISSN 1673-565X (Print); ISSN 1862-1775 (Online)
www.jzus.zju.edu.cn; www.springerlink.com
E-mail: jzus@zju.edu.cn

Experimental investigation on flow characteristics of a transverse jet with an upstream vortex generator*

Yan-hui ZHAO†[1], Jian-han LIANG[2], Shun-ping ZHANG[1], Hong-yu REN[1], Yu-xin ZHAO[2], Shun-hua YANG[1]

[1]*Science and Technology on Scramjet Laboratory, China Aerodynamics Research and Development Center, Mianyang 621000, China*

[2]*Science and Technology on Scramjet Laboratory, National University of Defense Technology, Changsha 410073, China*

†E-mail: mj311840@126.com

Received Aug. 19, 2019; Revision accepted Mar. 30, 2020; Crosschecked July 15, 2020

Abstract: This paper aims at probing the flow characteristics of a jet in supersonic crossflow (JISC) by installing a vortex generator (VG) upstream of the jet orifice. Nanoparticle planar laser scattering (NPLS) and stereo-particle image velocimetry (SPIV) technologies were employed to observe the flowfield, and three cases were designed for comparison. CASE0 stands for JISC without passive VG. In CASE1 and CASE2, VG is installed at 20 mm and 80 mm upstream away from the jet orifice, respectively. Transient flow structures show that two flow modes exist when the VG wake interacts with the JISC. In CASE1, vortices are induced from both sides of the jet plume because of the VG wake. This leads to a complex streamwise vortex system. Penetration and lateral diffusion are enhanced. In CASE2, intermittent large-scale eddies in the VG wake cause large streamwise vortices at the windward side of the jet. The penetration depth is also enhanced while the lateral diffusion is restrained. In addition, experimental results show that the penetration depth is approximately 8.5% higher in CASE1 than that in CASE0, and the lateral diffusion is larger by about 17.0%. In CASE2, the penetration is increased by about 26.2%, while the lateral diffusion is enhanced by just 0.5%.

Key words: Vortex generator (VG); Jet in supersonic crossflow (JISC); Penetration depth and lateral diffusion; Vortices structures

https://doi.org/10.1631/jzus.A1900392 **CLC number:** O358

1 Introduction

For scramjet combustors, high dynamic pressure of the incoming flow restricts the penetration of the wall injection. Flow characteristics of the jet in supersonic crossflow (JISC) have been researched and many conclusions reached (Karagozian, 2010; Mahesh, 2013). For example, slow growth rate of compressible shear layer in the supersonic flow causes poor fuel mixing (Papamoschou and Roshko, 1988; Huang et al., 2012, 2014). Mixing enhancement is necessary for boosting the fuel distribution to improve combustion capability, which benefits from the interaction of the jet plume due to multiport injection (Huang, 2016; Edalatpour et al., 2019). Gerdroodbary et al. (2016, 2017a) and Fallah et al. (2018) proposed a method to study the flow features by using computational fluid dynamics (CFD) and combining air jets with fuel injection. This shows that the flow features are extremely complex. However, the mixing rate is enhanced apparently because of the presence of the air jets in the supersonic combustor (Gerdroodbary et al., 2017b; Hassanvand et al., 2018). In addition, approaches such as importing slope, pylon, strut, and cavity have been put forward and compared in the

* Project supported by the National Natural Science Foundation of China (Nos. 91541203 and 51676204) and the Fenglei Youth Innovation Fund of China Aerodynamics Research and Development Center (No. PJD20170186)

ORCID: Yan-hui ZHAO, https://orcid.org/0000-0001-9716-3794

© Zhejiang University and Springer-Verlag GmbH Germany, part of Springer Nature 2020

literature (Lee, 2012; Sujith et al., 2013; Moradi et al., 2018). Bogdanoff (1994) pointed out that a high thrust coefficient and small pressure loss can be acquired using a mixing enhancement device with a small size blockage. Thus, a vortex generator (VG) is beneficial and feasible for fuel mixing.

The VG was first proposed by Bmynes and Tayler at United Airlines in 1947 (Huang and Lu, 2011). This method has been widely used to control the flow in the fields of aviation, automotive, shipbuilding, and other industrial fields. There are many different kinds of VG configrations. Zhong and Chen (1996) worked on a delta wing VG in subsonic flow. Relationships between the geometric parameters and the streamwise wake flow were analyzed, such as variations of the vorticity, vortex core radius, and vortex center height. Yan et al. (2012) carried out studies on the flow characteristics of the delta wing VG in supersonic flow, which includes momentum loss, Kelvin-Hemholtz (K-H) instability, and the generation and development of the vortex ring.

To study the flow characteristics with different VG configurations, schlieren, oil flow, wall pressure measurements, and laser Doppler anemometry (LDA) techniques were employed by Babinsky et al. (2009). Results showed that a strong counter-rotating vortex pair (CVP) emerged in the mainstream and mixing inside the boundary layer was improved. A low-momentum region was first observed at the downstream of the VG wake. It then moved upward from the wall and decayed gradually. The smaller the VG size, the faster the process developed. High-resolution nanoparticle planar laser scattering (NPLS) technology was used to observe the flow structure of the VG wake by Wang et al. (2012), and they concluded that the VG wake can be divided into two regions. Region 1 is located within a distance about one VG length away from the downstream VG, where the VG wake flow was dominated by CVP. As the VG wake developed downstream, the CVP gradually broke up and intermittent large-scale eddies formed. These evolved into typical structures of the wake flow in region 2.

The VG is commonly used in flow separation control (Szumowski and Wojciechowski, 2005), which has broad application prospects in subsonic and supersonic flow (Lin, 2002; Lee et al., 2011). Recently, this method was gradually extended to other applications. Zaman et al. (2010) carried out studies on the interaction between VG and inclined injection. The VG was conducive to wall cooling since the jet plume was maintained near the wall because of the streamwise vortices of the VG wake. Penetration of the JISC with an upstream VG was studied by Zhao et al. (2016) by experiment, which proved that both the configuration and position of the VG had effects on the penetration. The influence induced by the VG configuration was rather complicated. The penetration depth was increased as the distance between the VG and the jet orifice became large. Zhang et al. (2016) employed a CFD method to study fuel mixing in relation to the VG position. This showed that the mixing efficiency was improved as the VG was installed at either upstream or downstream of the jet orifice. The mixing efficiency of the jet plume with upstream VG was much higher. CFD methods were also employed by Saravanan and Suresh (2012) to study the mixing and combustion performance for a combustor with a VG. Results showed that the VG accelerated fuel mixing and ignition performance within the combustor. The vortex structures played a dominant role in the mixing process. However, the interaction mechanisms of VG wake flow and jet were not clear.

In this study, NPLS and particle image velocimetry (PIV)/stereo-particle image velocimetry (SPIV) are employed to observe the flowfield of the JISC. The experimental facilities and models are first described, and the flow features of the VG wake flow are studied for fundamental understanding. In order to study the fuel mixing enhancement of the VG, comparative experiments of the JISC with an upstream passive VG are designed and described. Jet penetration and lateral diffusion are summarized to reveal the merits of a VG. Interaction modes between the VG wake and transverse jet, and the mixing enhancement mechanisms are also analyzed. At last, the development of a vortex system is described.

2 Experimental facilities and observing methods

2.1 Wind tunnel and VG configuration

Since mixing enhancement with a VG is mainly implemented by interaction of the flow vortex and the

jet plume (Huang, 2018), in this paper the VG is placed upstream of the jet orifice. The VG configuration is shown in Fig. 1, where h is the height, α is the slope, and θ is the half cone angle.

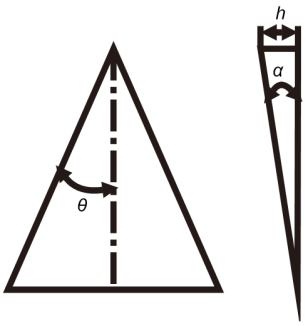

Fig. 1 Vortex generator configuration scheme

Slope (α) has effects on the bow shock of the VG front edge. This then leads to total pressure loss. According to the research of Anderson et al. (2006), half cone angle (θ) affects the CVP intensity of the VG wake, and height (h) of the VG directly determines the disturbance on the mainstream. In addition, since the control capability is not effective if the VG height is small, the height commonly occupies 10% or up to 70% of the boundary layer thickness. On the other hand, if the height chosen is too large, the total pressure loss of the mainstream is large. Hence, the height of the VG is selected as 3 mm ($h\approx0.6\delta_{0.99}$) since the thickness of the turbulent boundary layer is 5 mm in the experiments. Geometric parameters of the VG configuration in this study are listed in Table 1.

To study the flowfield of the JISC under control with upstream VG, a supersonic wind tunnel of the JISC is designed. The wind tunnel mainly consists of six sections, which are described carefully by Zhao et al. (2016). To obtain a parallel incident laser sheet, an optical reflector is added and installed as shown in Fig. 2. The reflected laser is parallel to the wall. In this way, the background generated by the wall can be eliminated. Manufactures of the nozzle and test section are integrated to eliminate shock waves. The experimental region is 120 mm×56 mm and the observing windows are distributed in three sidewalls to facilitate the optical measurements.

The jet orifice is linked with a gas container to ensure the stability of the jet total pressure. Pressure sensors are equipped in the gas container to monitor the pressures. Two unloaders are used to accurately adjust the jet total pressure. The pressure fluctuation of the gas container is less than 5% in the experiments. The jet total temperature is 300 K. The ratio of the jet to mainstream dynamic pressure is controlled by tuning the jet total pressure. Experimental parameters are listed as below in Table 2.

Table 1 VG geometric parameters

VG geometric parameter	Value
Slope, α (°)	9
Half cone angle, θ (°)	24
Height, h (mm)	3

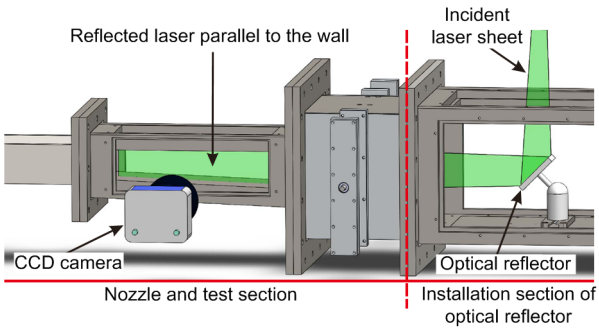

Fig. 2 Experimental section of wind tunnel
CCD: charge-coupled device

Table 2 Experimental parameters of wind tunnel mainstream and jet flow

Experimental parameter	Value
Mainstream static temperature, T_∞ (K)	123.1
Mainstream static pressure, P_∞ (Pa)	4488
Mainstream Mach number, Ma	2.68
Jet orifice diameter, d (mm)	2
Jet total temperature, T_{0j} (K)	300
Jet total pressure, P_{0j} (KPa)	300
Jet to mainstream dynamic pressure ratio, J	4.92

2.2 NPLS/SPIV system

Observing methods employed in this study include NPLS and SPIV technologies, which are conducted via the Dantec dynamics system. NPLS technology is based on the Rayleigh scattering principle, and SPIV technology depends on the Mie scatering principle. Detailed information of the NPLS system is described in (Tian et al., 2009; Zhao et al., 2009; Yi et al., 2010). A Schimpflug mount is employed to observe the flowfield of *yoz* slice. Fig. 3 illustrates the schematics of the observing methods. The Dantec dynamics system is employed for image recording and velocity measurements (Gerdroodbary

et al., 2017a) as shown in Fig. 4. It comprises a Vlite 500 Nd:YAG twin laser device (average power per pulse 400 mJ, max trigger rate 15 Hz), two FlowSense EO 11M CCD cameras (4000×2672 pixels, 12 bit), a synchronous controller for synchronization, and a Dell workstation where the control computer with DynamicStudio software is installed to control the whole system. A laser sheet lens is mounted at the laser exit to generate a diverging laser sheet. The diverged laser sheet is parallel to the *xoy* or *yoz* slice as shown in Fig. 3. TiO_2 particles with nominal diameter of 18 nm are chosen acting as the tracers in the flow measurement. The time interval t is set at 500 ns for the measured flowfield (freestream velocity 596 m/s). The particle image pairs are captured precisely by the cameras as the tracer particles in the measured flowfield are illuminated by the laser sheet. Thus, velocity fields can be calculated via corresponding algorithms.

Bias in the NPLS/PIV system is mainly caused by the behavior of following the tracer particles. However, this bias can be approximately evaluated using the particle diameter. Liu et al. (2016) developed an analyzed approach for the particle following behavior. Results showed that the particle diameter should be 20–50 nm in a high-speed flowfield (freestream velocity 1000 m/s). Comparing the incoming flow with previous studies (Tedeschi et al., 1999; Chen et al., 2012), the particle diameter is chosen to be about 300–500 nm. To be exact, the particle selection criteria proposed by Chen et al. (2017) are employed to evaluate it quantitatively. The bulk density of particles is 4230 kg/m^3, while the viscosity coefficient is 8.53×10^{-6} N·s/m^2 based on Sutherland's law. As a result, the particle diameter is 78–269 nm via their model. Otherwise, the particle diameter of the system employed in this study has been studied by Zhao et al. (2009). It is about 40.6 nm and ensures a promising following behavior.

3 Flow characteristics of the VG wake flow

3.1 Description of experimental observation

In order to give a clear description of the position of the observation slice, a coordinate system is established. The origin of the coordinate is placed at the rear edge of the VG as shown in Fig. 5. The position of the *xoy* observing slice is characterized by z coordinate, and the position of the *yoz* observing slice is characterized by x coordinate. Observing methods are listed in Table 3, which corresponds to each observing slice.

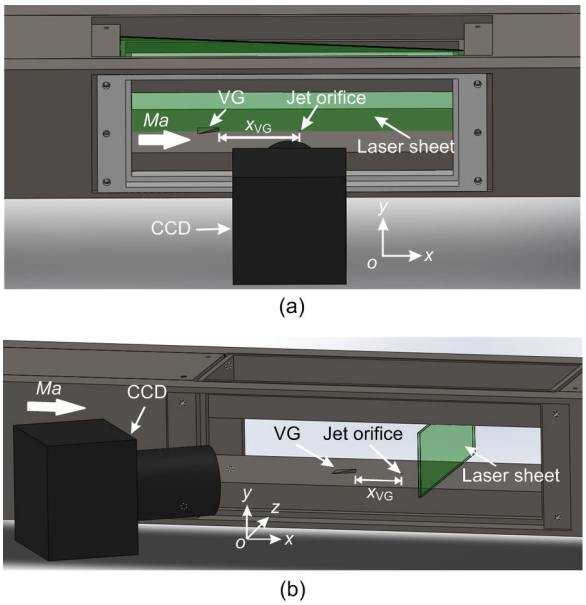

Fig. 3 Observing scheme of NPLS technology
(a) Observing scheme in *xoy* slice; (b) Observing scheme in *yoz* slice

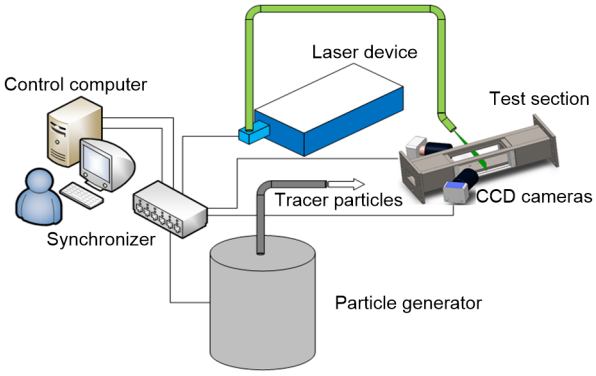

Fig. 4 Observing scheme of SPIV technology

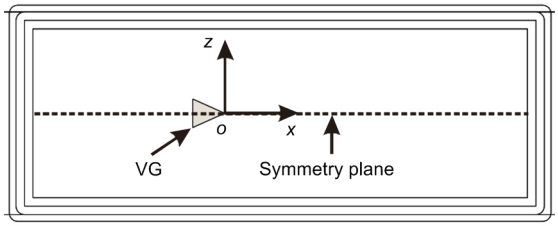

Fig. 5 Coordinate system of VG observation

Table 3 Observation details of VG wake flow

Slice	Observing method	Position of observing slice	Symbol of observing slice
xoy	NPLS	*z*=0 mm	XOY0
yoz	NPLS	*x*=5 mm,	YOZ5,
		x=20 mm,	YOZ20,
		x=80 mm	YOZ80
xoy	PIV	*z*=0 mm	XOY0
yoz	SPIV	*x*=20 mm,	YOZ20,
		x=80 mm	YOZ80

3.2 Experimental results of VG wake flow

Based on Gerdroodbary et al. (2017b), the wake flow of the delta wing VG can be divided into two regions as shown in Fig. 6a (Wang et al., 2012). A CVP is formed in region I and small-scale eddies emerge because of the strong K-H instability. Downstream, eddies begin to merge. This results in an intermittent large-scale eddy structure in region II. According to the experimental results in Fig. 6b, the length of region I is about 40 mm downstream of the VG. Since the incident laser from the rear produces a strong background light on the surface of the VG, the flow structures in region I are hardly distinguished. The intermittent large-scale eddy structure of region II is clearly recognized in transient gray images.

Fig. 7 displays the NPLS gray images of the VG wake in different *yoz* slices. The process of CVP development is deduced. A single vortex is formed on each side of the delta wing VG because of the strong pressure gradient. Then the two vortices get close to each other gradually, and form a CVP at the trailing edge VG. The dark region in Fig. 7a represents the low density region of the CVP. This reveals the core of vortices. The outer layer fluid of the wake starts to break up. The core area of the CVP reduces gradually as shown in Fig. 7b, and the inner region of the wake flow begins to break up. Streamwise vortices of the wake flow break down into small-scale eddies as shown in Fig. 7c.

By employing SPIV technology, the velocity with three components in the *yoz* slice can be obtained. The vorticity (ω) field can be calculated based on the velocity components (V_y and V_z) of y and z as shown by

$$\omega=\frac{\partial y}{\partial V_z}-\frac{\partial z}{\partial V_y}. \tag{1}$$

Velocity and vorticity fields of the VG wake flow are displayed in Fig. 8 (p.642). Every image is obtained by averaging 80 image pairs of PIV data. The CVPs are shown in Figs. 8c and 8d. One pair of the induced vortices is formed on both sides as shown in Fig. 8c. The surrounding fluid is mixed with the VG wake flow under the effects of those vortex structures. The overall velocity of the VG wake flow is higher in Fig. 8b than that in Fig. 8a, and the wake

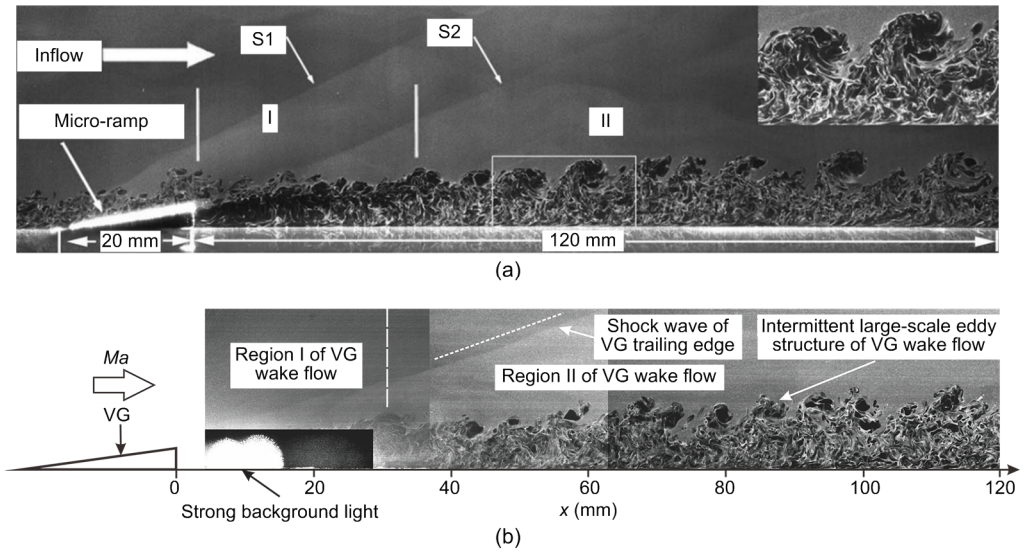

Fig. 6 Transient gray images of VG wake flow in XOY0: (a) research of Wang et al. (2012); (b) this study. Fig. 6a is reprinted from (Wang et al., 2012), Copyright 2012, with permission from American Institute of Physics

flow raises. According to the vorticity fields in Figs. 8c and 8d, induced vortices dissipate gradually as the mixing process proceeds.

Generally speaking, flow characteristics are different at the slices of YOZ20 and YOZ80. CVP is dominant in the developing process of the VG wake. The vortex structures derived from the CVP are more complicated at YOZ20. However, the wake flow possesses higher momentum at YOZ80. Thus, experiments are designed based on those differences.

4 Flow characteristics of JISC with upstream VG

4.1 Experimental setup of JISC with upstream VG

To introduce the experimental setup, a coordinate system is established. The coordinate origin is the center of the jet orifice as shown in Fig. 9. This locates at the symmetry plane of the VG. Both the VG position and observing slice are marked by this coordinate system.

As for the VG position, three cases are designed for comparative observation as shown in Table 4. The VG is not used in CASE0, which is regarded as a basic mode. Otherwise, VG was placed in two positions, representing different regions with different flow characteristics as discussed in the previous section. The VG is located 20 mm away from the center of the jet orifice in CASE1, and 80 mm away in CASE2.

The *xoy* and *yoz* observing slices are characterized by *z* and *x* coordinates, respectively. XOY0 stands for the *xoy* slice at *z*=0 mm. YOZ0 is the *yoz* slice at the center of the jet orifice. YOZ20, YOZ80, and YOZ100 represent the observing slices which are 20 mm, 80 mm, and 100 mm downstream from the jet orifice, respectively.

Table 4 Experimental cases

Experimental case	Relationship between VG and jet orifice
CASE0	There is no VG interacting with JISC
CASE1	VG is located 20 mm upstream of the jet orifice (x_{VG}=−20 mm)
CASE2	VG is located 80 mm upstream of the jet orifice (x_{VG}=−80 mm)

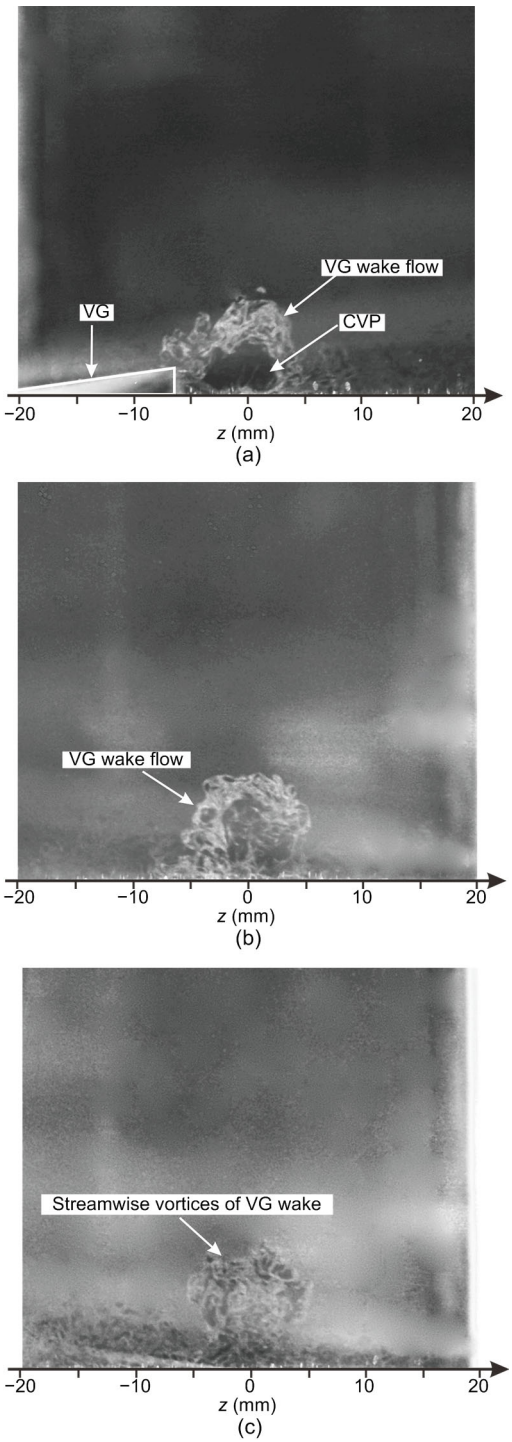

Fig. 7 Transient gray images of the VG wake flow in *yoz* slices
(a) YOZ5; (b) YOZ20; (c) YOZ80

NPLS and PIV/SPIV technologies are used to probe the detailed flowfields and velocity distributions of the observing regions. The observing slices

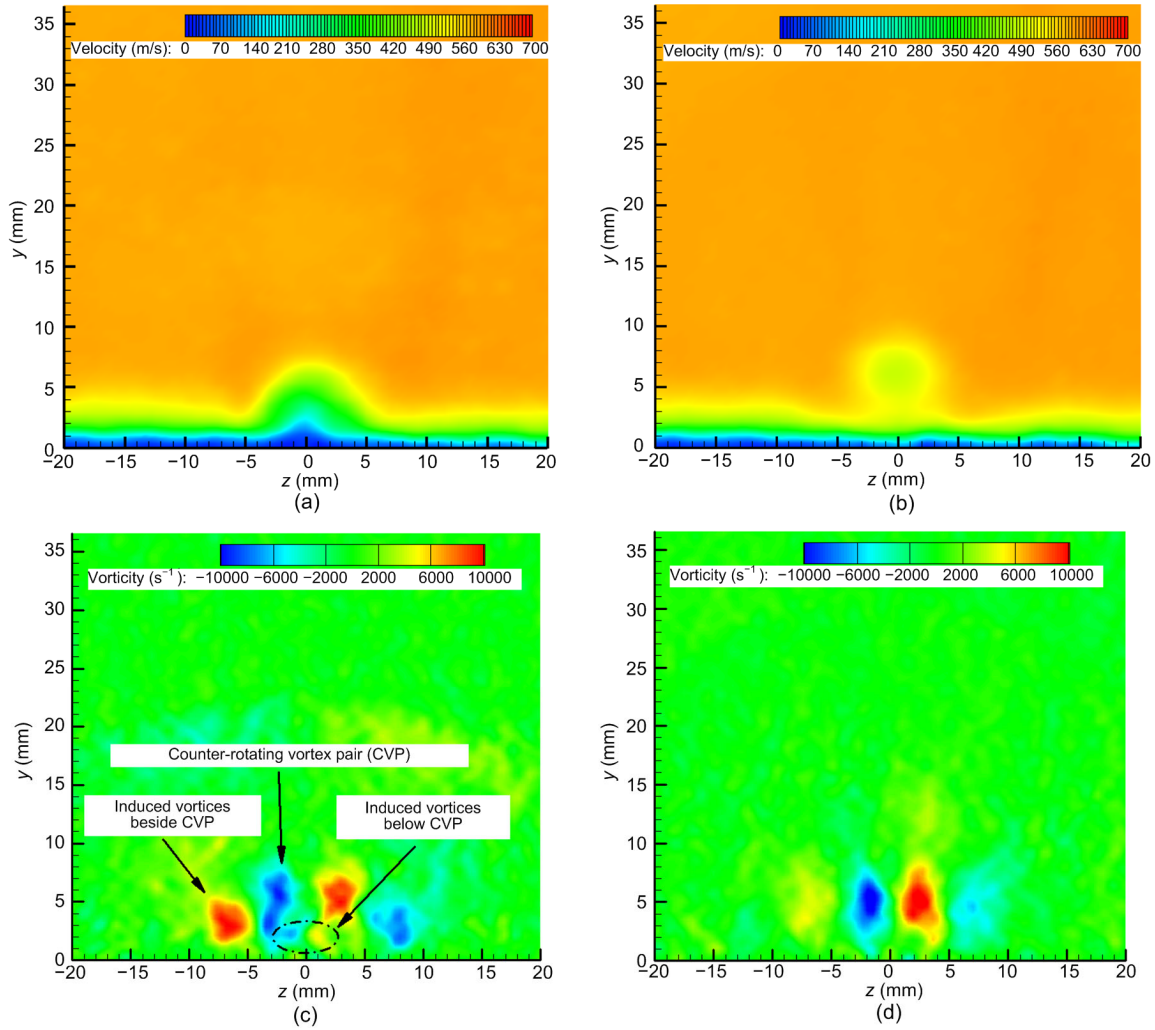

Fig. 8 Velocity and vorticity fields of VG wake flow in *yoz* slices

(a) Average scalar velocity field in YOZ20; (b) Average scalar velocity field in YOZ80; (c) Average vorticity field in YOZ20; (d) Average vorticity field in YOZ80

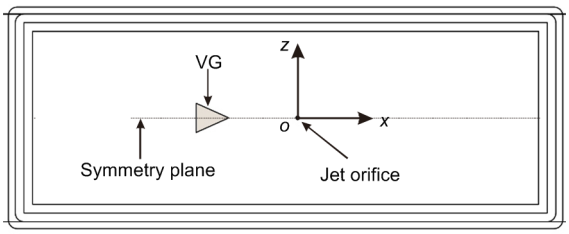

Fig. 9 Coordinate system of the JISC flowfield observation

corresponding to the optical measurement methods are shown in Table 5. The observing slices are the same for NPLS and PIV/SPIV technologies for all experiments except for CASE1. Unfortunately, since two cameras are requried for the SPIV observation, placements of the two cameras become inconvenient.

Table 5 Observing details of the JISC flowfield with upstream VG

Slice	Observing method	Location of observing slices	Symbol of observing slices
xoy	NPLS	z=0 mm	XOY0
yoz	NPLS	x=0 mm,	YOZ0,
		x=20 mm,	YOZ20,
		x=100 mm	YOZ100
xoy	PIV	z=0 mm	XOY0
yoz	SPIV	x=0 mm,	YOZ0,
		x=20 mm,	YOZ20,
		x=80 mm	YOZ80

In addition, placements of the cameras are limited in YOZ100. In order to gain acceptable velocity distribution, YOZ80 is used instead.

4.2 Transient flow structure of the JISC with upstream VG

The JISC flowfield of the three cases in Table 4 in XOY0 were observed. By analyzing the transient gray images of NPLS, a classic shock wave system, including shock waves of the VG leading edge and trailing edge, bow shock and barrel shock of the JISC, are clearly observed as shown in Fig. 10. The boundary layer of the mainstream flow is shown in Fig. 10a. However, in Fig. 10b, the region near the VG is sheltered by strong background light since the incident laser has a strong reflection from the surface of the VG. But the vortices of the VG wake flow are distinguishable. In Fig. 10c, the observation is quite good since the VG is far away from the observing region. Compared with Fig. 10a, the coherent large-eddy structures of the incoming flow are distinct. By enlarging the local graph in Fig. 10c, large-scale eddies of the VG wake enter the windward side of the jet through the bow shock, resulting in the deformation of the barrel shock. Strong disturbance is produced in the upwind shear layer of the jet plume.

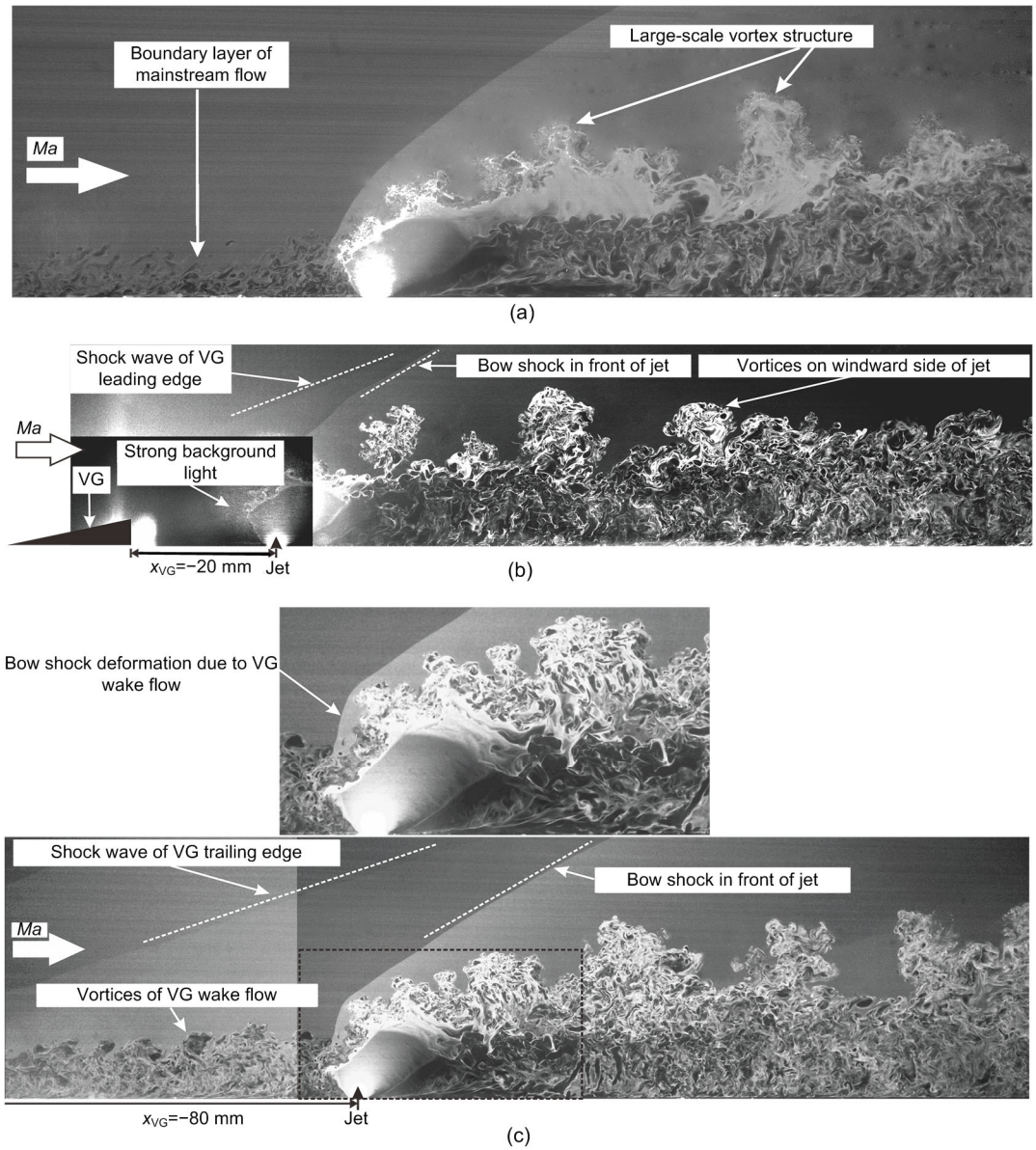

Fig. 10 Transient gray images of the JISC in different cases (XOY0)
(a) CASE0; (b) CASE1; (c) CASE2

Taking CASE0 as a fundamental test condition, transient gray images and the vorticity fields of *yoz* slices are obtained as shown in Fig. 11. The bow shock and barrel shock are obvious in Figs. 11a and 11c. The vortex structures of the jet plume change along with the streamwise development. The vortex

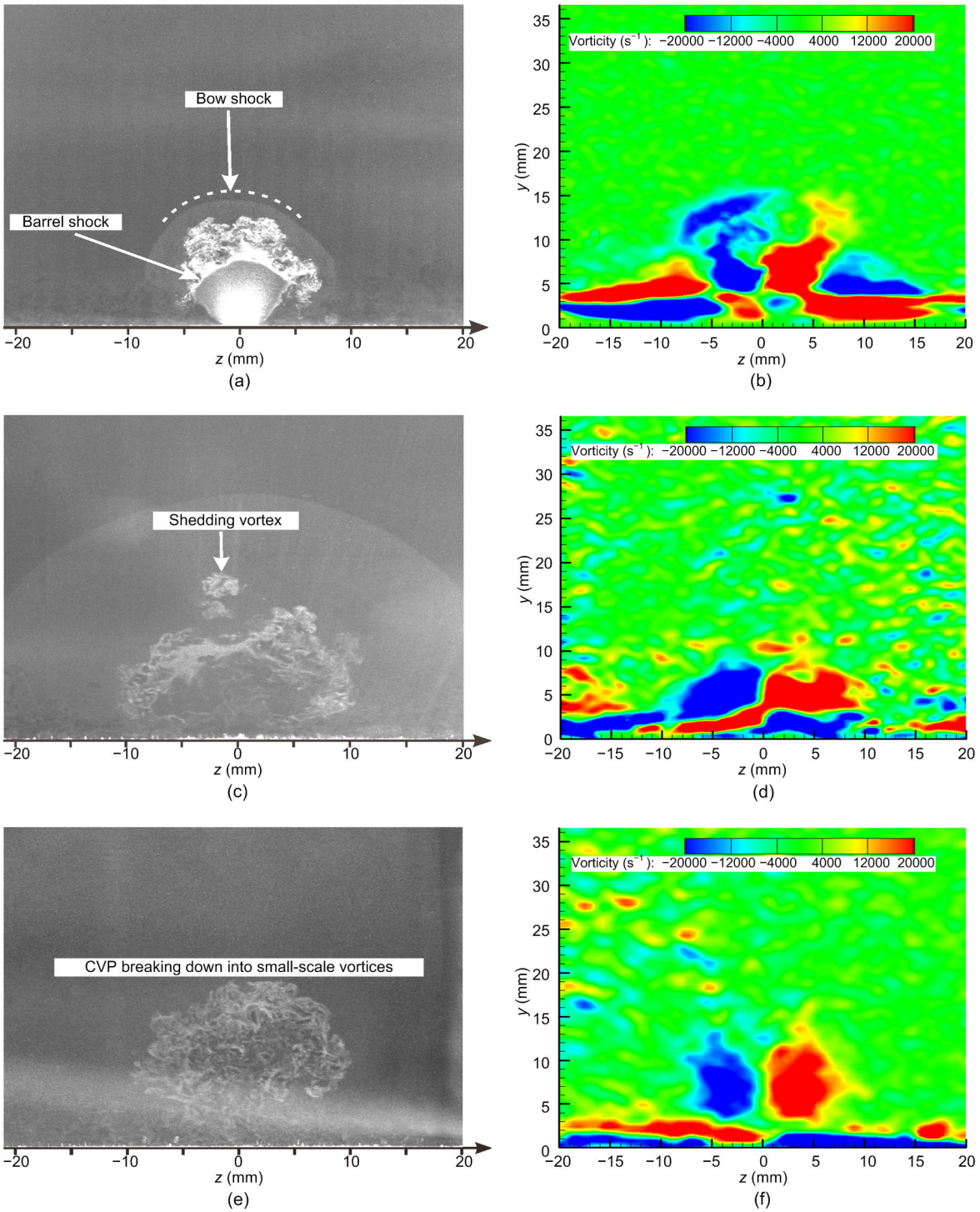

Fig. 11 Gray images and vorticity fields of JISC in different *yoz* slices (CASE0)

(a) Gray image of YOZ0; (b) Vorticity distribution of YOZ0; (c) Gray image of YOZ20; (d) Vorticity distribution of YOZ80; (e) Gray image of YOZ100; (f) Vorticity distribution of YOZ100

structures of the jet plume is rather complex in Figs. 11b and 11d. Typical kidney eddies of the CVP are shown in Fig. 11f.

In order to understand the 3D flow structures of the JISC flowfield with upstream VG, transient gray images and the vorticity fields of *yoz* slices are obtained as shown in Fig. 12. Comparing Fig. 12a with Figs. 11a and 12b, it is remarkable that two vortices roll up on both sides of the jet plume, and look like a pair of ears as displayed in CASE1. However, this type of vortex is not shown in CASE0 and CASE2. The two vortices grow during the developing

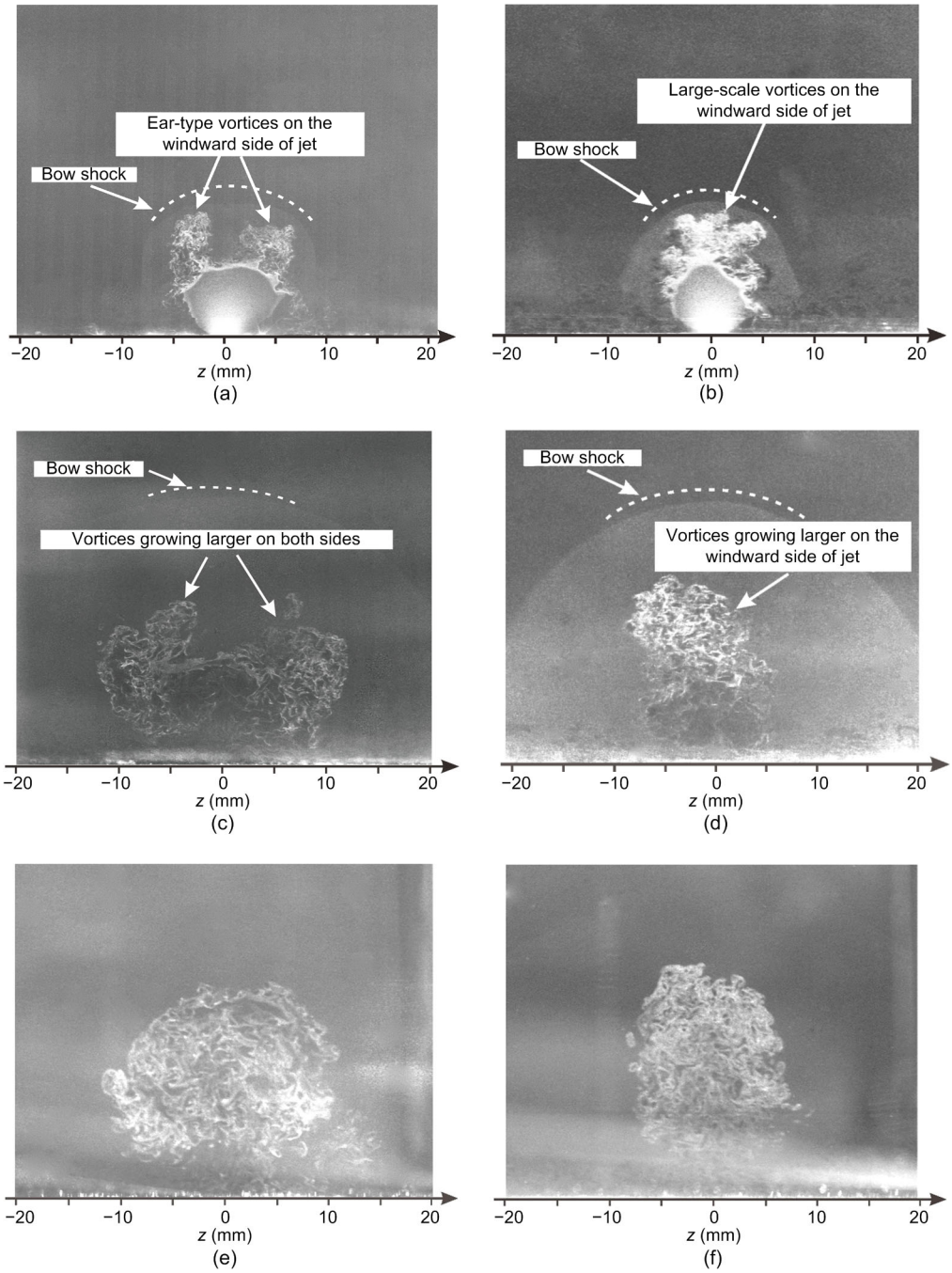

Fig. 12 Transient gray images of JISC with upstream VG in several *yoz* slices

(a) YOZ0 of CASE1; (b) YOZ0 of CASE2; (c) YOZ20 of CASE1; (d) YOZ20 of CASE2; (e) YOZ100 of CASE1; (f) YOZ100 of CASE2

process as shown in Fig. 12c. The vortices of the JISC merge together in Fig. 12e. Apparently, the ear-type vortices are caused by the complicated vortex structures of the VG wake flow in CASE1. The detailed mechanisms of its formation will be further studied in the future.

The VG wake flow interacting with the jet has high momentum in CASE2. The windward side of the jet is mainly affected by intermittent large-scale vortices. As a result, an overall large-scale vortex emerges in the upwind shear layer of the jet plume in Figs. 12b, 12d, and 12f. Considering the penetration and the lateral diffusion of jet plume, the ear-type vortices may have effects on them in CASE1. In CASE2, large-scale vortices clearly enhance the penetration, but the gain of the lateral diffusion is not distinct compared with that shown in Figs. 11c and 11e for CASE0.

Since K-H instability is quite strong on the windward side of the JISC, the vortices on the windward side of the jet change in the transient images. There are still some doubts about the existence of the ear-type vortices. Thus, a statistical analysis was performed based on 160 gray images under typical experimental conditions. Firstly, each gray image is binarized as shown in Figs. 13a and 13b corresponding to Figs. 12a and 12b. Then all the binarized images of the same condition are superimposed as shown in Figs. 13c and 13d. As a result, the gray levels of Figs. 13c and 13d represent the distribution probability of the jet plume. It is clear that the ear-type vortices play a typical role in CASE1 based on the regions with high probability. The distribution probability on the windward side of the jet performs like a crescent moon in CASE2. It can be concluded that the ear-type vortices of the transient flowfield are confirmed.

4.3 Penetration and lateral diffusion of JISC

Gray images of the JISC flowfield with upstream VG are captured via NPLS technology. The boundary of penetration and lateral diffusion can be extracted

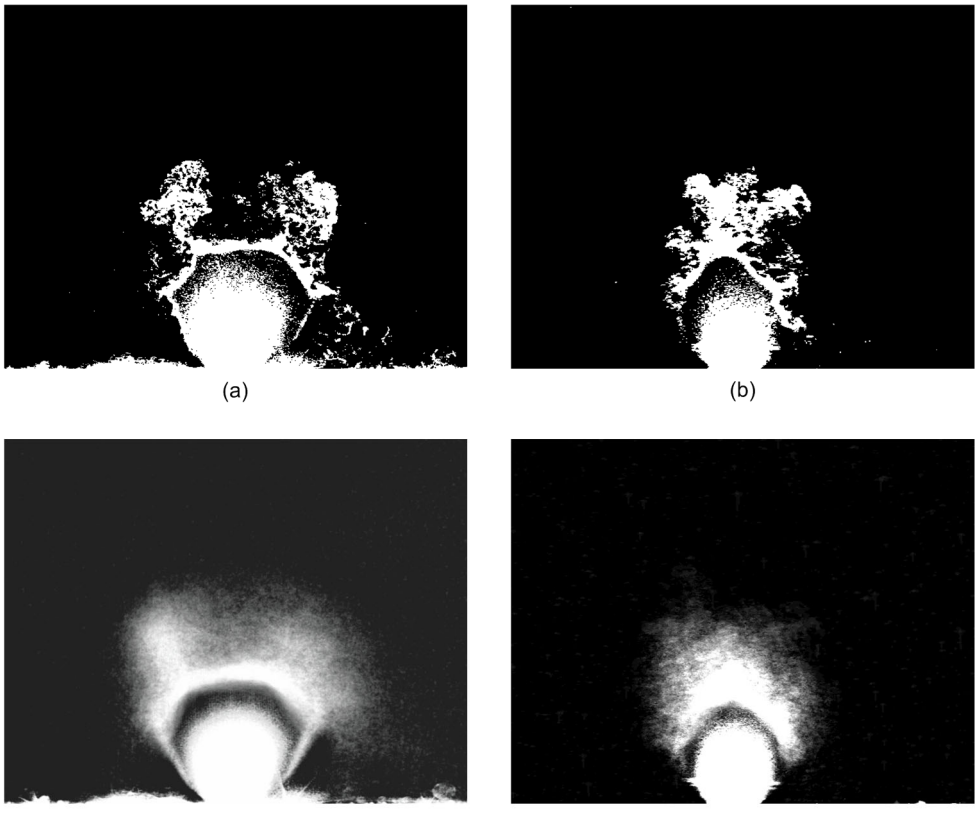

Fig. 13 Statistical analysis of the transient gray images in YOZ0
(a) Binary gray image of CASE1; (b) Binary gray image of CASE2; (c) Average image of CASE1; (d) Average image of CASE2

from each transient gray image via an edge detection method. Average values of the transient boundary are used to evaluate the penetration and lateral diffusion for the experimental cases. In all cases, 80 images are used to gain the average boundary shown in Fig. 14. As shown in Fig. 14a, the penetration depth at YOZ20 is 10.5% higher in CASE1 than that in CASE0, while it is 20.2% higher in CASE2 in comparison with CASE0. The increase becomes 8.5% and 26.2% at YOZ100. According to Fig. 14b, the lateral diffusion boundary in CASE1 is increased by 12.1% at YOZ20 and 17.0% at YOZ100 compared to CASE0. However, in CASE2 it is 20.3% less at YOZ20, while the deviation is 0.5% at YOZ100. Hence, penetration and lateral diffusion in CASE1 are both raised, benefitting from the ear-type vortices. On the other hand, the penetration is enhanced more significantly, which results from the induced vortices in CASE2, while the lateral diffusion is not improved.

4.4 Streamwise vortices development of JISC with upstream VG

In order to provide more information, the contour of scalar velocity is superimposed on the vorticity field in different *yoz* slices as shown in Fig. 15. Each is acquired from 80 image pairs.

The vortex structures in Figs. 15a and 15b are rather complex but perform similar features. The CVP is clearly dominant at YOZ0, inducing two pairs of vortices. One pair is generated on the outside of the CVP marked as V1 and V2, while the other emerges on the inside marked as V3 and V4. The vortex system is quite different from CASE0 shown in Fig. 11b, especially the scale of the vorticity. Induced vortices are weakened while the CVP is apparently enhanced. The locations of V3 and V4 are also different. They are supposed to be located below the CVP in the traditional JISC flowfield, but they lie on the inner side of the CVP in CASE1 and CASE2. Further information on the formation will be given in a following paper. This will relate, in large measure, to the interaction of the jet and VG wake.

As the vortex system develops, the induced vortices V3 and V4 merge together with the CVP at YOZ20, forming kidney eddies as displayed in Figs. 15c and 15d. The induced vortices V1 and V2 start to dissipate. However in CASE0, the kidney eddies are not formed at YOZ20, while the induced vortices are still seen to exist in Fig. 11d. As is seen from Figs. 15e and 15f, the kidney eddies develop and grow gradually. Meanwhile, the induced vortices almost dissipate completely, which is similar to that in Fig. 11f. It can be concluded that the VG wake flow has a great impact on the JISC vortex structures in the near-field mixing process. The kidney eddies of the CVP play a dominant role in the far-field mixing process.

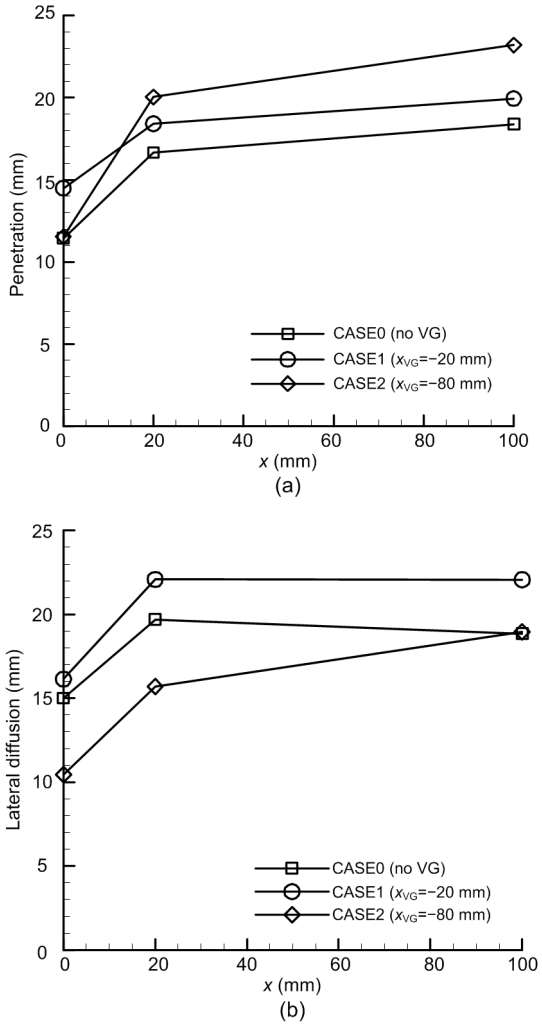

Fig. 14 Comparison of the penetration and lateral diffusion of JISC with upstream VG
(a) Penetration; (b) Lateral diffusion

5 Conclusions

In this study, the JISC flowfield controlled by the VG is studied via various experimental observing

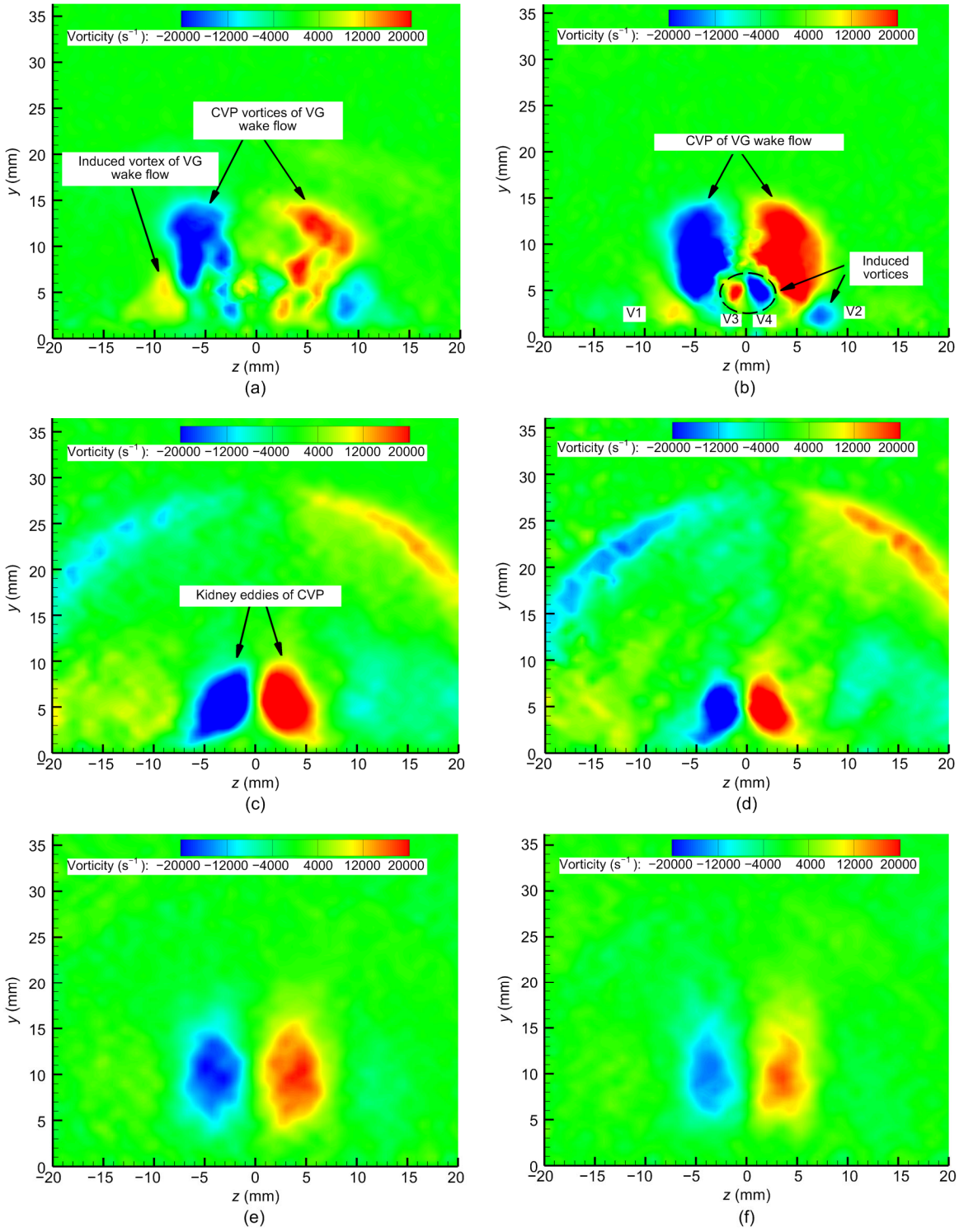

Fig. 15 Vorticity fields and velocity contour lines of JISC with upstream VG in different *yoz* slices

(a) YOZ0 of CASE1; (b) YOZ0 of CASE2; (c) YOZ20 of CASE1; (d) YOZ20 of CASE2; (e) YOZ80 of CASE1; (f) YOZ80 of CASE2

methods. Flow characteristics and interaction modes between the VG wake and the transverse jet are summarized. Penetration and lateral diffusion of transverse jet are extracted. The developments of

vortices are analyzed in order to reveal the mixing mechanisms. The main conclusions are:

1. Three experimental cases are designed. CASE0 is a basic test of JISC flowfield without VG. The distance between the jet orifice and the upstream VG is close in CASE1 while it is far in CASE2. As a result, two induced vortices are formed on both sides of the jet plume near the jet orifice in CASE1, which have the appearance of a pair of ears. In CASE2, intermittent large-scale eddies of the VG wake play a dominant role in induced vortices on the windward side of jet, resulting in a large-scale vortex.

2. Penetration and lateral diffusion of JISC rise simultaneously in CASE1. The increases of the penetration depth and lateral diffusion are 8.5% and 17.0% respectively in CASE1 compared to those in CASE0, while they are 26.2% and 0.5% in CASE2. Therefore, penetration is enhanced more significantly in CASE2, while the lateral diffusion is almost not improved. They are both related to the vortex structures of interaction modes.

3. Vorticity distribution indicates a complicated vortex system in CASE1, which is different from the JISC flowfield without the VG. A pair of induced vortices is formed on the inner side of the CVP, while it is supposed to be below the CVP. The formation of kidney eddies is promoted in advance. Further study is needed in the formation of the ear-type vortices and induced vortices.

Contributors

Jian-han LIANG designed the research. Yan-hui ZHAO and Shun-ping ZHANG processed the experiments. Yan-hui ZHAO wrote the first draft of the manuscript. Yu-xin ZHAO and Shun-hua YANG helped to organize the manuscript. Yan-hui ZHAO and Hong-yu REN revised and edited the final version.

Conflict of interest

Yan-hui ZHAO, Jian-han LIANG, Shun-ping ZHANG, Hong-yu REN, Yu-xin ZHAO, and Shun-hua YANG declare that they have no conflict of interest.

References

Anderson B, Tinapple J, Surber L, 2006. Optimal control of shock wave turbulent boundary layer interactions using micro-array actuation. Proceedings of the 3rd AIAA Flow Control Conference. https://doi.org/doi:10.2514/6.2006-3197

Babinsky H, Li Y, Ford CWP, 2009. Microramp control of supersonic oblique shock-wave/boundary-layer interactions. *AIAA Journal*, 47(3):668-675. https://doi.org/10.2514/1.38022

Bogdanoff DW, 1994. Advanced injection and mixing techniques for scramjet combustors. *Journal of Propulsion and Power*, 10(2):183-190. https://doi.org/10.2514/3.23728

Chen F, Liu H, Rong Z, 2012. Development and application of nanoparticle tracers for PIV in supersonic and hypersonic flows. Proceedings of the 50th AIAA Aerospace Sciences Meeting Including the New Horizons Forum and Aerospace Exposition.

Chen F, Liu H, Yang ZF, et al., 2017. Tracking characteristics of tracer particles for PIV measurements in supersonic flows. *Chinese Journal of Aeronautics*, 30(2):577-585. https://doi.org/10.1016/j.cja.2016.12.033

Edalatpour A, Hassanvand A, Gerdroodbary MB, et al., 2019. Injection of multi hydrogen jets within cavity flameholder at supersonic flow. *International Journal of Hydrogen Energy*, 44(26):13923-13931. https://doi.org/10.1016/j.ijhydene.2019.03.117

Fallah K, Gerdroodbary MB, Ghaderi A, et al., 2018. The influence of micro air jets on mixing augmentation of fuel in cavity flameholder at supersonic flow. *Aerospace Science and Technology*, 76:187-193. https://doi.org/10.1016/j.ast.2018.01.021

Gerdroodbary MB, Mokhtari M, Fallah K, et al., 2016. The influence of micro air jets on mixing augmentation of transverse hydrogen jet in supersonic flow. *International Journal of Hydrogen Energy*, 41(47):22497-22508. https://doi.org/10.1016/j.ijhydene.2016.08.185

Gerdroodbary MB, Amini Y, Ganji DD, et al., 2017a. The flow feature of transverse hydrogen jet in presence of micro air jets in supersonic flow. *Advances in Space Research*, 59(5):1330-1340. https://doi.org/10.1016/j.asr.2016.11.040

Gerdroodbary MB, Fallah K, Pourmirzaagha H, 2017b. Characteristics of transverse hydrogen jet in presence of multi air jets within scramjet combustor. *Acta Astronautica*, 132:25-32. https://doi.org/10.1016/j.actaastro.2016.11.041

Hassanvand A, Gerdroodbary MB, Fallah K, et al., 2018. Effect of dual micro fuel jets on mixing performance of hydrogen in cavity flameholder at supersonic flow. *International Journal of Hydrogen Energy*, 43(20):9829-9837. https://doi.org/10.1016/j.ijhydene.2018.03.230

Huang HB, Lu F, 2011. Research progress of vortex generator application. *Journal of Wuhan University of Technology* (*Transportation Science & Engineering*), 35(3):611-614 (in Chinese). https://doi.org/10.3963/j.issn.1006-2823.2011.03.043

Huang W, 2016. Transverse jet in supersonic crossflows. *Aerospace Science and Technology*, 50:183-195. https://doi.org/10.1016/j.ast.2016.01.001

Huang W, 2018. Mixing enhancement strategies and their

mechanisms in supersonic flows: a brief review. *Acta Astronautica*, 145:492-500. https://doi.org/10.1016/j.actaastro.2018.02.022

Huang W, Liu WD, Li SB, et al., 2012. Influences of the turbulence model and the slot width on the transverse slot injection flow field in supersonic flows. *Acta Astronautica*, 73:1-9. https://doi.org/10.1016/j.actaastro.2011.12.003

Huang W, Yang J, Yan L, 2014. Multi-objective design optimization of the transverse gaseous jet in supersonic flows. *Acta Astronautica*, 93:13-22. https://doi.org/10.1016/j.actaastro.2013.06.027

Karagozian AR, 2010. Transverse jets and their control. *Progress in Energy and Combustion Science*, 36(5):531-553. https://doi.org/10.1016/j.pecs.2010.01.001

Lee S, Loth E, Babinsky H, 2011. Normal shock boundary layer control with various vortex generator geometries. *Computers & Fluids*, 49(1):233-246. https://doi.org/10.1016/j.compfluid.2011.06.003

Lee SH, 2012. Mixing augmentation with cooled pylon injection in a scramjet combustor. *Journal of Propulsion and Power*, 28(3):477-485. https://doi.org/10.2514/1.b34220

Lin JC, 2002. Review of research on low-profile vortex generators to control boundary-layer separation. *Progress in Aerospace Sciences*, 38(4-5):389-420. https://doi.org/10.1016/s0376-0421(02)00010-6

Liu H, Chen F, Li XJ, et al., 2016. Practices and challenges on PIV technology in high speed complex flows. *Journal of Experiments in Fluid Mechanics*, 30(1):28-42 (in Chinese). https://doi.org/10.11729/syltlx20150069

Mahesh K, 2013. The interaction of jets with crossflow. *Annual Review of Fluid Mechanics*, 45(1):379-407. https://doi.org/10.1146/annurev-fluid-120710-101115

Moradi R, Mahyari A, Gerdroodbary MB, et al., 2018. Shape effect of cavity flameholder on mixing zone of hydrogen jet at supersonic flow. *International Journal of Hydrogen Energy*, 43(33):16364-16372. https://doi.org/10.1016/j.ijhydene.2018.06.166

Papamoschou D, Roshko A, 1988. The compressible turbulent shear layer: an experimental study. *Journal of Fluid Mechanics*, 197:453-477. https://doi.org/10.1017/S0022112088003325

Saravanan G, Suresh C, 2012. Numerical simulation of mixing enhancement in scramjet using micro vortex generator. *Procedia Engineering*, 38:3969-3976. https://doi.org/10.1016/j.proeng.2012.06.454

Sujith S, Muruganandam TM, Kurian J, 2013. Effect of trailing ramp angles in strut-based injection in supersonic flow. *Journal of Propulsion and Power*, 29(1):66-78. https://doi.org/10.2514/1.b34532

Szumowski A, Wojciechowski J, 2005. Use of vortex generators to control internal supersonic flow separation. *AIAA Journal*, 43(1):216-218. https://doi.org/10.2514/1.5741

Tedeschi G, Gouin H, Elena M, 1999. Motion of tracer particles in supersonic flows. *Experiments in Fluids*, 26(4):288-296. https://doi.org/10.1007/s003480050291

Tian LF, Yi SH, Zhao YX, et al., 2009. Study of density field measurement based on NPLS technique in supersonic flow. *Science in China Series G: Physics, Mechanics and Astronomy*, 52(9):1357-1363. https://doi.org/10.1007/s11433-009-0180-4

Wang B, Liu WD, Zhao YX, et al., 2012. Experimental investigation of the micro-ramp based shock wave and turbulent boundary layer interaction control. *Physics of Fluids*, 24(5):055110. https://doi.org/10.1063/1.4719146

Yan YH, Li Q, Liu CQ, et al., 2012. Numerical discovery and experimental confirmation of vortex ring generation by microramp vortex generator. *Applied Mathematical Modelling*, 36(11):5700-5708. https://doi.org/10.1016/j.apm.2012.01.015

Yi SH, Tian LF, Zhao YX, et al., 2010. Aero-optical aberration measuring method based on NPLS and its application. *Chinese Science Bulletin*, 55(31):3545-3549. https://doi.org/10.1007/s11434-010-4104-5

Zaman KBMQ, Rigby DL, Heidmann JD, 2010. Inclined jet in crossflow interacting with a vortex generator. *Journal of Propulsion and Power*, 26(5):947-954. https://doi.org/10.2514/1.49742

Zhang YJ, Liu WD, Wang B, et al., 2016. Effects of microramp on transverse jet in supersonic crossflow. *Acta Astronautica*, 127:160-170. https://doi.org/10.1016/j.actaastro.2016.05.032

Zhao YH, Liang JH, Yan TT, 2016. Penetration characteristics and optimization of transverse jet on condition of vortex generator. *Journal of Aerospace Power*, 31(4):800-806 (in Chinese). https://doi.org/10.13224/j.cnki.jasp.2016.04.005

Zhao YX, Yi SH, Tian LF, et al., 2009. Supersonic flow imaging via nanoparticles. *Science in China Series E: Technological Sciences*, 52(12):3640-3648. https://doi.org/10.1007/s11431-009-0281-3

Zhong YC, Chen X, 1996. Effects of geometric parameters of submerged delta vortex generator on vortex. *Journal of Aerospace Power*, 11(3):241-244 (in Chinese). https://doi.org/10.13224/j.cnki.jasp.1996.03.005

中文概要

题　目：喷孔上游涡流发生器诱导下的横向射流流动特性研究

目　的：通过在喷孔上游安装涡流发生器（VG）来研究超声速横向射流（JISC）的流动特性。采用纳米粒子平面激光散射（NPLS）和空间粒子图像测速（SPIV）技术对流场进行观测，并设计三种工况

进行对比实验，以研究横向射流的流动特性。

创新点： 1. 采用 NPLS 和 SPIV 为实验观测手段，定量化地研究涡流发生器对超声速来流的穿透深度和横向扩散的影响；2. 根据实验观测结果展示涡流发生器与横向射流相互作用的流场特性，揭示涡流发生器的混合增强机理。

方　法： 1. 采用 NPLS 流场进行观测，获得瞬态流场灰度图（图 6、7 和 10~12），并分析不同观测平面的瞬态流场结构；2. 基于瞬态流场灰度图，通过边缘检测和统计分析方法，提取射流穿透深度和横向扩散边界（图 14），并对涡流发生器的混合增强效果进行分析；3. 采用 SPIV 技术对流场进行观测，获得多个观测截面的平均速度场，并根据速度场计算涡量场（图 8、11 和 15），揭示射流流向涡的涡量分布。

结　论： 1. 在设计的三个实验工况中，CASE0 是横向射流基本工况；与 CASE0 相比，CASE1 中的 VG 在喷孔附近的羽流两侧产生了两个诱导涡，在形态上形成了一个耳朵形涡结构；CASE2 中 VG 尾流的间歇性大尺度涡对射流迎风侧的诱导涡起主导作用，产生了一个大尺度流向涡。2. 与 CASE0 相比，CASE1 中射流的穿透深度和横向扩散边界分别增加了 8.5%和 17.0%，而 CASE2 中的穿透深度和横向扩散边界分别增加了 26.2%和 0.5%；因此，在 CASE2 中，穿透深度的增加更显著，而横向扩散没有明显改善，这与相互作用模式的涡结构特性有关。3. 涡量分布表明，CASE1 中存在一个复杂流向涡系统，且 VG 的尾流在射流反转旋涡对（CVP）的内侧形成了一对诱导涡，而在 CASE0 中，诱导涡应该在 CVP 的下方。4. 根据多个 *yoz* 截面的涡量场分布可以发现，VG 促进了射流肾形涡的形成和发展。

关键词： 涡流发生器；超声速来流中的横向射流；穿透深度与横向扩散；涡结构